

Design, modeling, and optimization of compliant tensegrity fabrics for the reduction of turbulent skin friction

Haoxiang Luo^{*} and Thomas R. Bewley

Dept. of MAE, UC San Diego, La Jolla, CA 92093, USA

ABSTRACT

In this project, we have designed a new type of flexible surface, which we call a *tensegrity fabric*, and simulated the interaction of this flexible surface with a near-wall turbulent flow. The fabric is constructed by weaving together both members in tension (tendons) and members in compression (bars) to form a plate-class tensegrity structure, then covering this discrete flexible structure with a continuous flexible membrane. We have modeled the flow/structure interaction by coupling a spectral Direct Numerical Simulation (DNS) code resolving the (continuous) turbulent flow system and an efficient structural dynamics code which simulates directly the motion of the (discrete) extensive, small-scale, and interconnected tensegrity structure. The structural dynamics code used was developed by Prof. Robert Skelton's lab at UC San Diego. An immersed boundary method is used to capture the effect of the moving boundary in the DNS, and a simple tessellation strategy is used to lump the distributed fluid forces (skin friction and pressure) acting on the membrane onto the nearby nodes of the tensegrity structure. Our ultimate goal is to use this new simulation tool to optimize the design of the tensegrity structure (specifically, the orientation, stiffness, mass, and damping of each of the individual tendons and bars in the unit cell upon which the tensegrity structure is based). Our objective in this optimization is to tune the compliance properties of the fabric in such a way as to reduce the skin-friction drag induced at the flow/structure interface by weakening the vortices near the wall in the overlying turbulent flow.

Keywords: compliant surface, turbulent drag reduction, tensegrity, immersed boundary method

1. INTRODUCTION

1.1. Compliant surfaces for turbulent drag reduction

In the region immediately adjacent to a wall, turbulent flows are dominated by small vortices, commonly referred to as "coherent structures", which have a characteristic and predictable scale and orientation. These vortices are responsible for transporting a significant component of momentum towards the wall, thereby causing high drag and a loss of system efficiency in a variety of practical applications of engineering interest. Numerous numerical experiments have shown that, if the interaction of these near-wall coherent structures with the wall can somehow be mitigated, the drag of the turbulent flow will be significantly reduced.

A variety of strategies have been investigated previously in order to manipulate the near-wall vortices and obtain drag reduction. Strategies explored to date include both active control, such as blowing/suction at the wall and prescribed wall motions, and passive control, such as polymer additives, riblets, and compliant coatings. Reviews of recent advances in the active and passive control of wall-bounded turbulent flows are contained in Bewley, Moin, & Temam (2001) and Gad-el-Hak (1996).

Inspired by the highly-efficient swimming capability of dolphins, it has been hypothesized that a well-designed compliant surface might be able to reduce the intensity of near-wall turbulence and thereby reduce the skin friction of a turbulent flow. However, except for Kramer's first observations (1957, 1960) of skin friction reductions with compliant coatings in his pioneering experiments, few laboratories had achieved measurable drag reductions with compliant coatings when applied to fully turbulent flows. A notable exception is the recent compliant surface experiments of Choi *et al.* (1997), in which a 5% drag reduction in a fully turbulent flow is reported.

The current lack of convincing laboratory demonstrations of turbulent drag reduction due to surface compliance might likely be because a surface with the correct compliance properties has simply not yet been tested. In the linear setting, the response characteristics of a surface to an overlying flow is a function of the streamwise and spanwise wavelengths and the

^{*}hluo@ucsd.edu; phone 1 858 822-3729; fax 1 858 822-3107

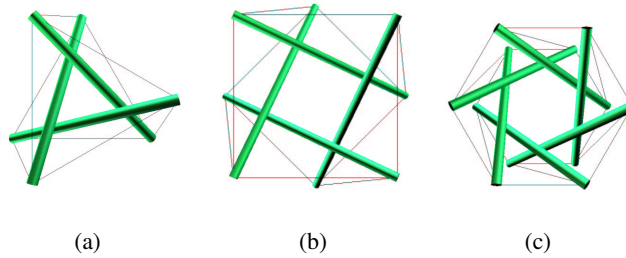


Figure 1. Stable tensegrity unit cells. (a) Three-bar cell, (b) four-bar cell, and (c) six-bar cell.

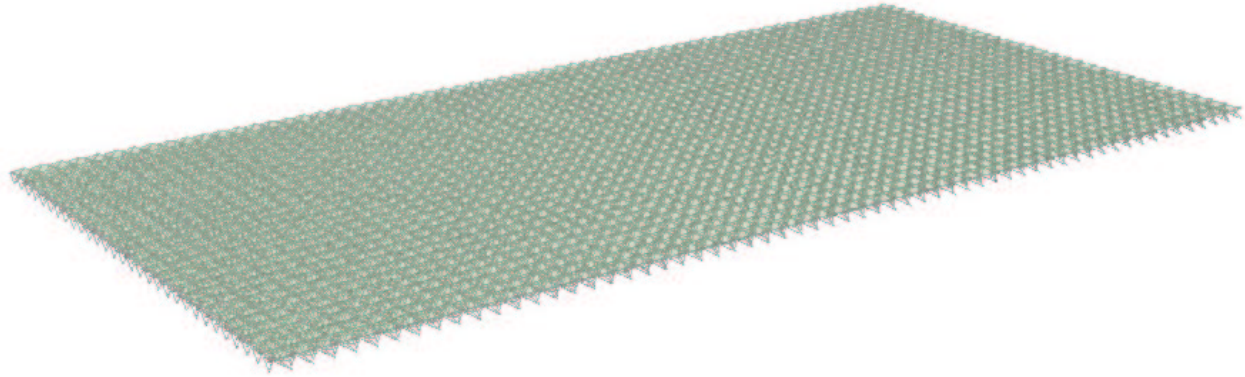


Figure 2. A tensegrity fabric with a membrane stretched over the top.

temporal frequency of the flow perturbations near the wall, and is a very high-dimensional optimization problem. Though we know roughly that the desired surface should extract energy from the dominant flow perturbations which seed further flow instabilities, or perhaps at least to scramble the phase of such perturbations, it is difficult, if not impossible, to extend this rough notion into an appropriate material specification. In order to design an appropriate compliant surface to test, a high-dimensional optimization problem must first be solved.

1.2. Tensegrity fabrics

The compliant surface model we are considering is based on a special structural paradigm known as *tensegrity*, which is a stable pretensioned collection of structural members in tension (“tendons”) and members in compression (“bars”). The structure is mass efficient because no structural member experiences a bending load. The same structural paradigm appears to form the molecular foundation for spider fibers (Ingber 1997, 1998), which is nature’s strongest material per unit mass (several times stronger per unit mass than steel). In close collaboration with Prof. Skelton’s group, we have been able to parameterize completely several families of flexible stable tensegrity structures with broad or infinite extent in two directions, which we refer to as *plate-class* structures. These structures are constructed by interconnection of stable unit cells (see, e.g., Figure 1) in such a manner as to fill the plane, as depicted in Figure 2. By designing the fabric in such a manner, failures of individual members do not compromise the integrity of the entire tensegrity fabric, but simply lead to a modest deformation of the nearby cells, thus providing robustness in the overall system.

Several previous studies (see, e.g., Carpenter *et al.*, 1985, 1990; Endo *et al.*, 2002; Xu *et al.*, 2003) have used spring-supported viscoelastic-elastic plates/membrane to model a compliant wall (Figure 3). One of the reasons that we have chosen the tensegrity paradigm in the present work is that it provides us with several additional degrees of freedom to optimize in our design. A tensegrity fabric may be formed by interconnecting stable 3-bar, 4-bar, or 6-bar unit cells. The geometry, the size of the unit cell, and the stiffness, mass, damping, and orientation of each of the members within the unit cell may be tuned such that the overall fabric responds to the overlying flow in a desired fashion.

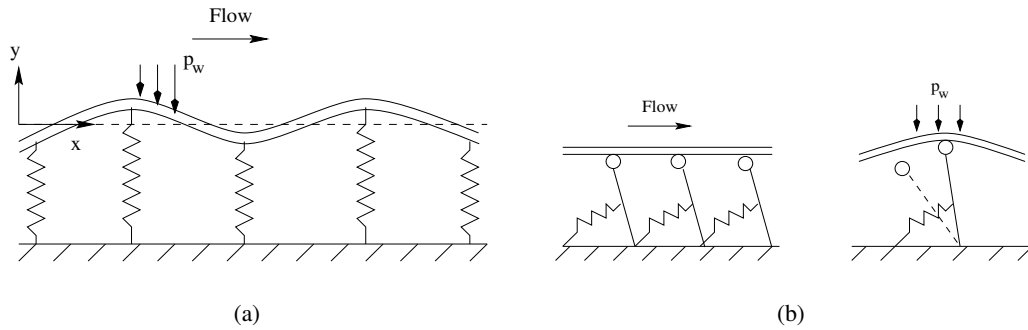


Figure 3. Spring-supported compliant wall models. (a) Isotropic model, (b) anisotropic model. (Adapted from Carpenter *et al.*, 1985, 1990).

Another motivation for using a tensegrity structure is that all bars in such a structure are inclined, so the entire structure may respond to both normal and tangential loads. In the spring-supported viscoelastic-elastic plate/membrane model, the wall responds to pressure fluctuations only (see Figure 3a). However, the capacity of the surface to respond to friction (tangential) forces in addition to pressure (normal) forces (see Figure 3b) is particularly attractive, and might lead to new opportunities to produce a drag-reducing compliant surface (Bewley & Protas, footprints). An anisotropic compliant wall was first presented by Grosskreutz (1971) and later analyzed theoretically by Carpenter & Morris (1990), and has been shown to provide particular advantages with regard to the stabilization of transitional flows. The present work explores a generalization of this strategy and its application in the turbulent regime.

The theoretical anisotropic wall model illustrated in figure 3(b) is constructed with a thin plate supported by inclined lever arms and springs. Under small-amplitude pressure fluctuations, the horizontal and vertical displacements of the ends of the lever arms may be related in such a way that a negative Reynolds shear stress is generated and thereby the production of turbulence near the wall is reduced (Carpenter *et al.*, 1990). In the present work, we hope to orient the structural members in the tensegrity fabric in such a way that the flow/structure interaction will produce a similar stabilizing effect.

1.3. Representation of the flow-structure interface

Two techniques have been identified to form the flow-structure interface between the (continuous) flow above and the (discrete but small scale) structure below. The first, as depicted in Figure 2, is to simply stretch a flexible membrane over the top of the tensegrity structure, transmitting the force generated by the flow to the top nodes of the structure. Another option includes the attachment of small mechanical “scale” to each surface node of the tensegrity structure, mimicking the scales on a shark’s skin. In our simulation model, we assume that the force from the flow is transmitted to the top nodes of the structure in a simple fashion approximating the latter technique. The surface is tessellated into small “patches” surrounding each node. The friction and pressure forces induced by the flow are then integrated over each patch and lumped to the associated node of the tensegrity structure.

2. NUMERICAL SIMULATION OF TURBULENT CHANNEL FLOW WITH A MOVING BOUNDARY

2.1. Immersed boundary method

We use a Direct Numerical Simulation (DNS) code to model the incompressible flow in a channel. To accommodate the time-varying boundary, an immersed boundary method is used to avoid an expensive boundary-conforming grid reconstruction at each time step. Peskin (1977) first developed the immersed boundary method and applied it to biological systems such as the flow of blood in a heart. Several variations of this method have since been developed and applied to a variety of complex problems with time-varying geometries. The method is sometimes used in situations where there is a real “immersed” interface between two different fluids. For example, Pozrikidis (1995) implemented a method with a pointwise body force distribution over the interface for solving the problem of the deformation of liquid drops in a shear

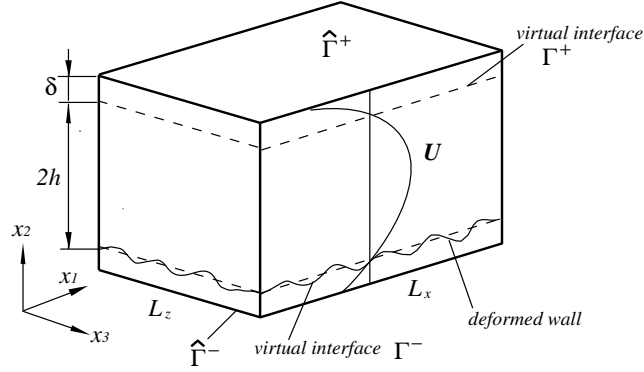


Figure 4. Diagram of the computational domain

flow. The method is also commonly used in situations in which there is no actual fluid on the other side of the boundary, but (for computational reasons) an artificial flow domain is defined so that the time-varying physical boundary of the fluid system essentially becomes “immersed”. For example, Goldstein (1993) presented a feedback scheme for the body force, and simulated the turbulent flow through a ribbed channel. Fadlun (2000) applied a direct forcing scheme proposed by Mohd-Yusof (1997) to solve the flow problem inside an IC piston/cylinder assembly at high Reynolds number.

The basic idea of the immersed boundary method is that a time-invariant regular grid is used despite the boundary’s complexity. Flow fields on both sides of the “immersed” boundary are solved, even if one of these fields should be considered as artificial. Body forces are added within this artificial region to enforce the desired boundary conditions and dynamic motions of at the immersed interface.

In the present system, the flow is confined by the deformed and time-varying walls in a channel. We thus augment the physical flow domain, assuming there exists an artificial flow outside the channel walls with the same physical properties (mass, density) as the actual flow between the channel walls. Thus, the physical walls of the channel become “immersed”. In this project, we consider small amplitude wall deformations only, $\eta^+ < 5$, where η denotes the wall displacement and $+$ denotes distance in viscous units. To accommodate the small boundary variations, we adopt the direct forcing scheme mentioned above so that evaluation of the body force can be avoided when solving the Navier-Stokes equation. However, we still need to calculate the divergence of the body force when solving the Poisson equation for the pressure field.

2.2. DNS flow model

The augmented flow domain is illustrated in the figure 4. Two extra slabs are added at the top and the bottom. We allow only the bottom interface to deform so we may use the upper interface as a reference. The lower wall deforms in such a manner that the total volume of the physical domain does not change. The physical domain is denoted as Ω , the augmented domain as $\hat{\Omega}$. Γ^+ , Γ^- stand for the upper and lower immersed boundaries, respectively, and $\hat{\Gamma}^+$, $\hat{\Gamma}^-$ stand for the upper and lower external boundaries, respectively. The channel size is $(0, L_x) \times (-h - \delta, h + \delta) \times (0, L_z)$; without loss of generality, we assume $h = 1$. The mean flow is aligned in the x_1 direction.

The flow, for the physical domain and the artificial domain alike, is governed by the incompressible Navier-Stokes equation

$$\frac{\partial \mathbf{u}}{\partial t} + \nabla(\mathbf{u}\mathbf{u}) + \nabla p = \nu \Delta \mathbf{u} - \mathbf{i}P_x + \mathbf{f} \quad (1)$$

$$\nabla \cdot \mathbf{u} = 0,$$

where p is the pressure divided by the density ρ and ν is the kinetic viscosity. The variables x_i are normalized by the half-width of the channel h , \mathbf{u} is normalized by the mean friction velocity $u_\tau \triangleq (\overline{\tau_w}/\rho)^{1/2}$, and t is normalized by h/u_τ . The Reynolds number based on the mean friction velocity and the half channel width is defined by $Re_\tau \triangleq u_\tau h/\nu$. $\mathbf{i}P_x$ is the time-varying but spatially-uniform pressure gradient in the x_1 direction, which is adjusted in such a way as to maintain constant mass flux in the physical domain at every time step.

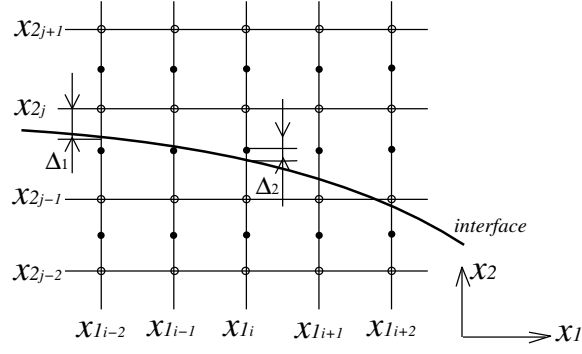


Figure 5. Diagram of the deformed wall and the staggered grid

Direct forcing \mathbf{f} is applied in the virtual interface region such that the no-slip and no-penetration boundary conditions

$$\mathbf{u} = \dot{\boldsymbol{\eta}}, \quad (2)$$

is satisfied at each time step, where $\boldsymbol{\eta}$ is the vertical motion of the wall. The horizontal motions are ignored since the wall deformation is very small.

Periodic boundary conditions are assumed in the streamwise (x_1) and spanwise (x_3) directions. The external boundaries are modeled with

$$u_2 = 0, \quad \frac{\partial u_3}{\partial x_2} = 0, \quad \text{on } \hat{\Gamma}^\pm; \quad \frac{\partial u_1}{\partial x_2} \Big|_{\hat{\Gamma}^\pm} = \text{constant} = \overline{\tau_w} \Big|_{\hat{\Gamma}^\pm}. \quad (3)$$

The “slip” condition is used to simplify the dynamics of the flow in the artificial region outside the immersed channel walls. These choices provide an approximately linear mean profile across the immersed interface, which improves accuracy in the numerical implementation.

2.3. Numerical scheme

The computational scheme is based on the numerical method adopted for the turbulent flow prediction in Bewley, Moin, & Temam (2001). Details about the temporal discretization can be found in Akselvoll & Moin (1995). The scheme may be summarized as follows:

(1) A pseudospectral method is used for terms containing x_1 and x_3 derivatives, and a finite difference method is used for terms containing x_2 derivatives. A uniform, collocated grid is used in the x_1 and x_3 directions, and a stretched, staggered grid is used in the x_2 direction.

(2) A low-storage 3rd order Runge-Kutta scheme is used for the temporal evolution. The derivatives with respect to the homogeneous directions (x_1 and x_3) are treated explicitly in time, and the derivatives with respect to the inhomogeneous direction (x_2) are computed with the implicit Crank-Nicolson method in time.

Using our “direct forcing” scheme, we do not calculate the external force \mathbf{f} when solving the NS equation. Instead, we solve the equation with the no-slip/no-penetration constraint $g(\mathbf{u}) = 0$. In the discrete implementation, the positions of the interface are generally not coincident with the grid points (see, e.g., Figure 5), so the constraint $g(\mathbf{u}) = 0$ represents a numerical interpolation procedure to approximate the velocities at the immersed interface.

In the present work, we use an interpolation procedure based on Taylor series expansions. We use linear interpolation for the streamwise and spanwise velocity components and quadratic interpolation for the wall-normal velocity component.

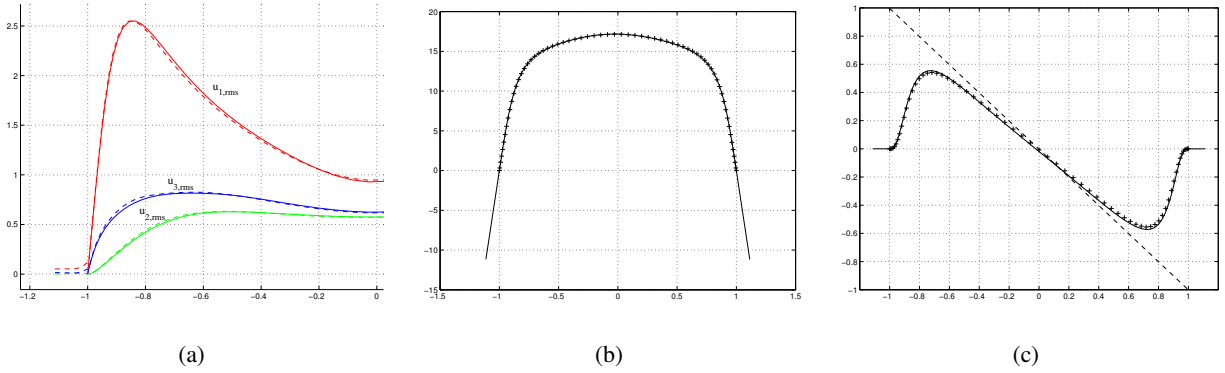


Figure 6. Comparison of selected time-averaged statistics from simulations of the immersed boundary method and the regular domain. (a) Profiles of RMS velocity fluctuations; (b) mean velocity profiles; (c) profiles of Reynolds stress and total stress. Solid —, simulation from the immersed boundary method; dashed (---) in (a) and plus sign (+) in (b) and (c), simulation from the regular domain.

The velocities on the grid points that are close to the interface are constrained to satisfy the formulae

$$\begin{aligned}
 u_{1,j-\frac{1}{2}} + \frac{u_{1,j+\frac{1}{2}} - u_{1,j-\frac{1}{2}}}{x_{2,j+\frac{1}{2}} - x_{2,j-\frac{1}{2}}} \Delta_2 &= 0, \\
 u_{2,j} + \frac{u_{2,j+1} - u_{2,j-1}}{2(x_{2,j+1} - x_{2,j-1})} \Delta_1 + \frac{1}{2} \frac{u_{2,j+1} - 2u_{2,j} + u_{2,j-1}}{(x_{2,j+1} - x_{2,j-1})^2} \Delta_1^2 &= \dot{\eta}, \\
 u_{3,j-\frac{1}{2}} + \frac{u_{3,j+\frac{1}{2}} - u_{3,j-\frac{1}{2}}}{x_{2,j+\frac{1}{2}} - x_{2,j-\frac{1}{2}}} \Delta_2 &= 0,
 \end{aligned} \tag{4}$$

where Δ_1 and Δ_2 are illustrated in Figure 5.

The external force \mathbf{f} is directly evaluated by the NS equation.

$$\mathbf{f} = \frac{\partial \mathbf{u}}{\partial t} + \nabla(\mathbf{u}\mathbf{u}) + \nabla p - \nu \Delta \mathbf{u} + \mathbf{i}P_x. \tag{5}$$

Since the external force \mathbf{f} is not divergence free, the term $\nabla \cdot \mathbf{f}$ is included when solving Poisson equation for the pressure.

2.4. Code validation

We first test our DNS code with the immersed boundary method on the canonical channel flow problem in which both immersed walls are stationary and not deformed. The Reynolds number is $Re_\tau = 100$ and $42 \times 64 \times 42$ Fourier modes are used (i.e., $64 \times 64 \times 64$ dealiased collocation grid points). We compared the statistics with a simulation that does not have an immersed boundary and has been extensively validated by Bewley, Moin, & Temam (2001). Selected statistics are shown in Figure 6. The correspondence of two simulations in the physical domain region is fairly good. In Figure 6(b), we can see that the mean velocity profile is extended linearly into the two artificial regions, so the linear interpolation approximation for u_1 and u_3 at the interface regions is justified. The profile of the pressure fluctuations (not shown here) in the immersed boundary simulation shows there is a jump across the immersed interface, which implies that the interface provides something of a “barrier” between the real flow and the artificial flows.

The second test is the active wall motion control. The control scheme is that, based on measurements of the vertical velocity somewhere close to the wall, same amount of opposite control velocity as the measurements is applied at the wall.

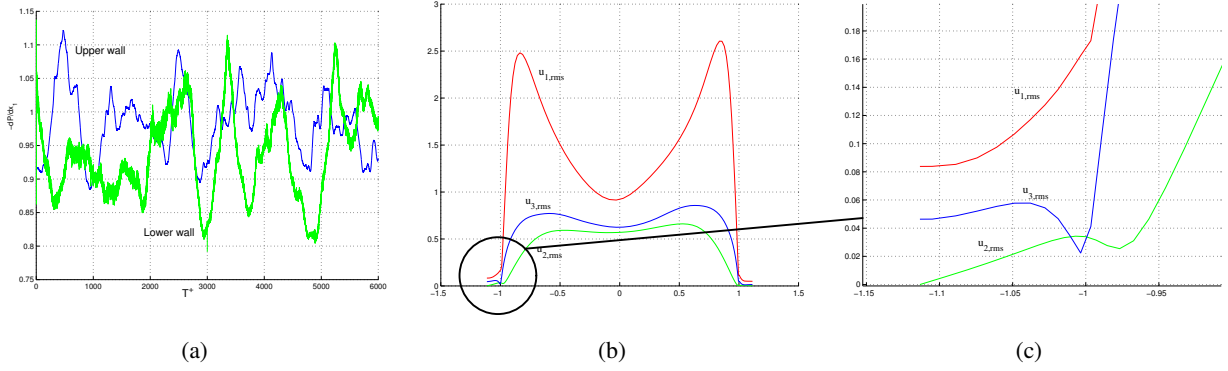


Figure 7. Statistics for deforming wall opposition control using the immersed boundary method. (a) History of drag; (b) profiles of RMS velocity fluctuations; (c) zoom-in view of the lower wall region in (b).

Choi *et al.* (1994) first investigated the scheme and obtained more than 20% drag reduction. The control actuation they used was unsteady blowing/suction. Inspired by this research, Endo *et al.* (2000) employed vertical wall motion actuation based on the same kind of measurements. The simulations they did with $Re_\tau = 150$ and $\eta_{rms}^+ \approx 1$ showed that drag was reduced about 10%. Then Kang and Choi (2000) did the similar work with $Re_\tau = 140$ and $\eta_{max}^+ \leq 5$, and the drag was reduced up to 13% ~ 17%.

In our test, we prescribe the wall motion as follows

$$\frac{\partial \eta}{\partial t} = -\alpha u_2|_{x_2^+=15} - \beta \eta, \quad \alpha = \frac{\max\{u_2|_{x_2^+=15}\}}{V_{max}}, \quad (6)$$

where V_{max} is a pre-defined constant. The formula means that the velocity of the wall is opposite to the vertical velocity component (u_2) 15 viscous unit away from the wall with the amount scaled by a factor α to reduce the control intensity. The second term is a damping term used by Endo *et al.* (2000). The purpose is to slow down wall movement and reduce the deformation magnitude when the displacement is large.

Figure 7 shows some statistics from the simulation for $Re_\tau = 100$ and $\eta_{rms}^+ \approx 0.03$. Time-averaged drag on the two immersed walls shows that drag on the lower wall is about 4.5% less than that on the upper wall, which is quite slight compared to what Endo and Kang have obtained. Note that the control we applied is very weak. Currently we are still tuning the code to accommodate stronger control actuation.

From the profile of the *RMS* of velocity fluctuations (Figure 7(b)), we can see clearly that the streamwise velocity fluctuation intensity is lower at the bottom wall side compared the upper wall side. If we zoom in the region close to the lower wall (Figure 7(c)), we see that the minima of vertical velocity fluctuation is shifted away a little away from the wall. This is a typical feature of the opposition control which represents a virtual barrier above the wall preventing the high momentum flow from being transported to the wall, and thereby drag reduction is obtained.

3. DYNAMICS OF THE TENSEGRITY FABRIC

3.1. Periodic configuration

To maintain consistency with the channel flow model, which is assumed to be periodic in x and z , the tensegrity fabric needs to be configured with periodic boundary conditions. The fabric we have chosen for the compliant wall model has periodic patterns which, in the undeformed structure, repeat themselves cell by cell in the two horizontal directions. The 4-bar-unit plate-class tensegrity structure is particularly convenient for this study since its two periodic directions are orthogonal; this structure has been selected for our initial calculations. We may choose the period length of the pattern according to the flow channel size and define appropriate number of the unit cells in one period. Figure 8 illustrates how the periodic connection of the fabric is configured in one direction; extension to the other direction is trivial. In the figure, the “ghost cells” in the right-most column are defined to emulate the motion of the cells in the left-most column.

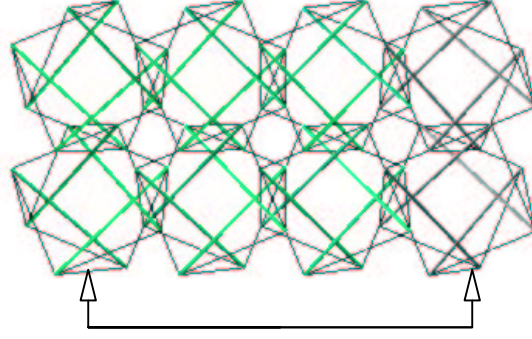


Figure 8. Periodic connection in one direction

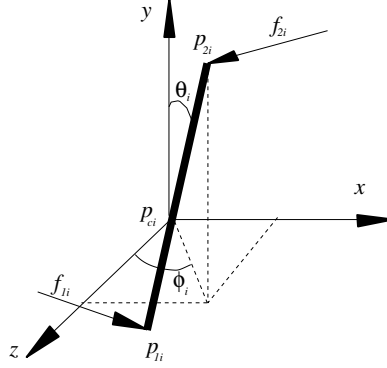


Figure 9. Dynamics of the i 'th bar

3.2. Dynamics

In the tensegrity structure, all bars are subject to nodal forces only, which include tendon forces and external forces excited by the overlying turbulent flow. Prof. Skelton's group has conducted an extensive study of a convenient mathematical representation of such a structure, characterizing its topology, statics and dynamics (Skelton, *et al.*, 2001). Their work is extended here in a straightforward manner to the tensegrity fabric, which is spatially periodic in the x and z directions. In this work, we only briefly summarized the mathematical model. The generalized coordinate is used for the bar system. For the i 'th bar, if not constrained, its coordinate vector is $\mathbf{x}_i = \begin{bmatrix} \mathbf{p}_{c_i} \\ \mathbf{q}_i \end{bmatrix}$, where \mathbf{p}_{c_i} is the 3d coordinate of the center of mass and $\mathbf{q}_i = [\theta_i \ \phi_i]^T$ consists of the two Euler angles (Figure 9).

The dynamics of the unconstrained bar system, which is basically a collection of each bar's dynamics, can be written as

$$M(\mathbf{q})\ddot{\mathbf{x}} + C(\mathbf{q}, \dot{\mathbf{q}})\dot{\mathbf{q}} = \tau = H^T(\mathbf{q})\mathbf{f}, \quad (7)$$

together with the periodic condition

$$\dot{\mathbf{x}}_g = G\dot{\mathbf{x}}, \quad (8)$$

where M is the inertia matrix, C is the Coriolis and centripetal matrix, τ is the generalized force vector which equals to the nodal force vector \mathbf{f} multiplied by a transformation matrix H^T , \mathbf{x}_g is the generalized coordinate for the ghost bars, and G is a projection matrix which does nothing but copy dynamics of the appropriate bars selected from the whole system to the ghost bars.

In a tensegrity structure, all bars are interconnected by tendons. In the dynamics equation, the interconnection appears in two places. First, the nodal force vector \mathbf{f} is calculated from

$$\mathbf{f} = S\mathbf{t} + \mathbf{f}_e \quad (9)$$

where S is the connectivity matrix, \mathbf{t} is the tendon force vector and \mathbf{f}_e is the external force vector (generated by the flow in our case). Consisting only of 1's, -1's, and 0's, the connectivity matrix S defines to which nodes each tendon is connected.

Second, the tendon force \mathbf{t} is based on Hookes law, but for tension only. So it depends on the coordinate of the bar system. Damping force is incorporated into tendon force and it is modeled as linear damping which is proportional to the tendons' relative velocities. Therefore the tendon force vector \mathbf{t} is a function of bar system coordinate \mathbf{x} , velocity $\dot{\mathbf{x}}$, and the coordinate of ghost bars \mathbf{x}_g since we have tendons connecting ghost bars and real bars.

In the first phase of this project, we consider a fabric with a single layer (multiple layers setting may be employed in future). Therefore, all the bars in the single stage are grounded, so only two Euler angles are used for the coordinate of each bar and those redundant tendons connecting between the grounded nodes are removed for simplicity.

3.3. Normalization

The normalization procedure may be done by considering the linear acceleration equation of a bar subject to pressure disturbance from the flow. For dimensional analysis, we don't need to consider the skin friction which has the same dimension of normalized pressure multiplied by the flow density. The linear acceleration equation for the i 'th bar can be written as

$$\rho_{b_i} l_{b_i} \ddot{\mathbf{p}}_{c_i} = \sum_j [k_j (l_j - l_{0_j}) - \xi_j \dot{l}_j] \bar{\mathbf{e}}_j + \rho p_w A_0, \quad (10)$$

where ρ_{b_i} is mass per unit length of the bar, l_{b_i} is the length of the bar, k_j is the stiffness of the j 'th tendon that is connected to the bar, l_j , l_{0_j} are the length and rest length of the tendon, respectively, $\bar{\mathbf{e}}_j$ is the normalized tendon vector, p_w is the hydrodynamic pressure (divided by the flow density ρ) acted on the surface by the overlying flow, and A_0 is area of the membrane patch on which the external pressure is lumped.

If we use L for the length scale, T for the time scale, it can be easily seen the following dimension similarities are valid

$$\rho_{b_i} \sim \rho p T^2, \quad \xi_j \sim \frac{\rho_{b_i} L}{T}, \quad k_j \sim \frac{\rho_{b_i} L}{T^2}.$$

Since in the flow model, L is normalized by the half channel width h , ρp is normalized by ρu_τ^2 , T is normalized by h/u_τ , then the final normalization is

$$\rho_{b_i} \sim \rho h^2, \quad \xi_j \sim \rho h \nu Re_\tau, \quad k_j \sim Re_\tau^2 \frac{\rho \nu^2}{h}. \quad (11)$$

4. SIMULATING THE DYNAMICS OF THE FLOW-STRUCTURE INTERFACE

The current flow/structure simulation involves combining the DNS channel flow code (in Fortran90) with the immersed boundary method and the tensegrity code based on the work of Prof. Skelton's group (written in C/C++ and combined with Matlab C/C++ Math Library). The two codes are coordinated by Message Passing Interface (MPI) and run in parallel. A visualization tool using OpenGL (a common graphics library) has been written to visualize the flow/structure interaction process (as illustrated in Figure 10).

As mentioned previously, in our simulation model, we assume that the force from the flow is transmitted to the top nodes of the structure in a simple fashion. The top surface of the tensegrity fabric is tessellated into small "patches" associated with each node whose position does not coincide with the Cartesian grid point in the flow model. During each computation time step, the pressure and/or skin-friction fluctuations integrated over each patch are lumped onto the top nodes of the tensegrity fabric. The displacements and velocities of the top nodes, which are somewhat scattered, are interpolated onto the uniform grid so they could be fed back to the flow system as the compliant boundary condition.

The average spanwise spacing the near-wall vortices (coherent structures) is about 50 in viscous length. To mitigate the detrimental effect of the vortices with favorable flow-structure interaction, the tensegrity cells are made smaller than that average spacing. For example, in our flow-structure simulation with $Re_\tau = 100$, the width of each tensegrity cell is approximately 14 viscous units, and thus there are a few cells beneath each near-wall coherent structure.

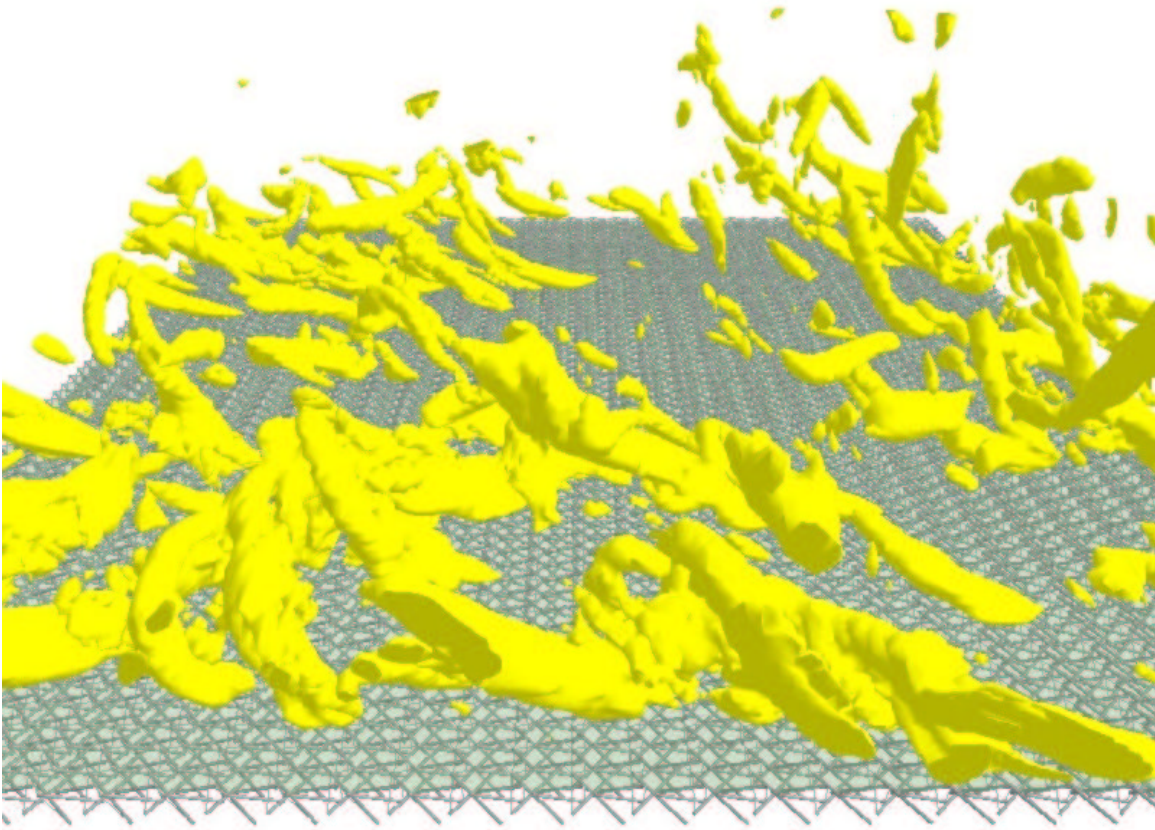


Figure 10. A simulation of the mutual interaction of a turbulent flow and a compliant tensegrity fabric separated by a flexible membrane attached to the top nodes of the tensegrity fabric. The viewpoint is from upstream and slightly above the wall; the flow direction is into the page. See <http://turbulence.ucsd.edu/gallery/tensegrity.html> for an animation of this result.

5. CONCLUSIONS

The present work has built a discrete and periodic compliant wall model based on a new design for a tensegrity fabric. The dynamics of this fabric is modeled with a large ODE system based on previous work in Skelton's lab. To account for the compliance of the wall, an immersed boundary method is used to simulate a moving boundary without requiring grid reconstruction at each time step. So far, this method can capture the effect of small wall motion fairly well. Two large codes have been coupled together and some flow-structure simulations with relatively low Reynolds number have been performed. The flow/structure interaction process may be visualized using a graphical visualization tool written in house.

The statistics of the flow/structure interaction will be collected and analyzed to better understand the relevant physical mechanisms. Parameters that we may adjust in this "passively-controlled" system include the stiffness, mass, damping, and orientation (within certain now well-defined constraints) of each of the members in the unit cell upon which the tensegrity structure is based. In the final phase of this work, we will explore the utility of adjoint-based techniques to optimize these several structural parameters of the tensegrity fabric in an attempt to achieve a reduction of turbulent skin friction.

ACKNOWLEDGMENTS

The authors gratefully acknowledge a close collaboration with Prof. Robert Skelton's group at UC San Diego, without which this work would not have been possible.

REFERENCES

1. AKSELVOLL, K. & MOIN, P. 1995 Large eddy simulation of turbulent confined coannular jets and turbulent flow over a backward facing step. *Report TF-63*, Thermosciences Division, Dept. of Mech. Eng., Stanford University.
2. BEWLEY, T.R., MOIN, P., & TEMAM, R. 2001 DNS-based predictive control of turbulence: an optimal benchmark for feedback algorithms. *J. Fluid Mech.* **447**, 179-225.
3. BEWLEY, T.R., & PROTAS, B. Skin-friction and pressure: the footprints of turbulence. *Footprints*.
4. CARLSON, H.A., BERKOOZ G., & LUMLEY J.L. 1995 Direct numerical simulation of flow in a channel with complex, time-dependent wall geometries: A pseudospectral method. *J. Comp. Phys.* **121**, 155-175.
5. CARPENTER, P.W., MORRIS, P.J. 1990 The effect of anisotropic wall compliance on boundary-layer stability and transition. *J. Fluid Mech.* **218**, 171-223.
6. CARPENTER, P.W., GARRAD, A.D. 1985 The hydrodynamic stability of flow over Kramer-type compliant surfaces. I. Tollmien-Schlichting instabilities. *J. Fluid Mech.* **155**, 465-510.
7. CHOI, H., MOIN, P., & KIM J. 1994 Active turbulence control for drag reduction in wall-bounded flows. *J. Fluid Mech.* **262**, 75-110.
8. CHOI, K.-S. *et al.* 1997 Turbulent drag reduction using compliant surfaces. *Proc. Royal Soc. Lond. A* **453**, 2229.
9. ENDO, T., KASAGI, N., & SUZUKI, Y. 2000 Feedback control of wall turbulence with wall deformation. *Int. J. Heat and Fluid Flow* **21**, 568-575.
10. ENDO, T., HIMENO, R. 2002 Direct numerical simulation of turbulent flow over a compliant surface. *J. Turbulence* **3**, 007.
11. FADLUN, E.A., VERZICCO, R., ORLANDI, P., & MOHD-YUSOF, J. 2000 Combined immersed-boundary finite-difference methods for three-dimensional complex flow simulations. *J. Comp. Phys.* **161**, 35-60.
12. GAD-EL-HAK, M. 1996 Modern developments in flow control. *Appl. Mech. Rev.* **49** (7), 365-379.
13. GOLDSTEIN, D., HANDLER, R., & SIROVICH, L. 1993 Modeling a no-slip flow boundary with an external force field. *J. Comp. Phys.* **105**, 354-366.
14. INGBER, D.E. 1997 Tensegrity: The architectural basis of cellular mechanotransduction. *Annual Review of Physiology* **59**, 575-599.
15. INGBER, D.E. 1998 Architecture of life. *Scientific American* January, 48-57.
16. KANG, S. & CHOI, H. 2000 Active wall motions for skin-friction drag reduction. *Phys. Fluids* **12**, 3301-3304.
17. KRAMER, M. O. 1957 Boundary-layer stabilization by distributed damping. *J. Aero. Sci.* **24**, 459-460.
18. KRAMER, M. O. 1960 The dolphin's secret. *New Scientist* **7**, 1118-1120.
19. MOHD-YUSOF, J. 1997 Combined immersed-boundary/B-spline methods for simulations of flow in complex geometries. *CTR Annual Research Briefs, Center for Turbulence Research, NASA Ames/Stanford Univ.* 317-327.
20. PESKIN, C. S. 1977 Numerical analysis of blood flow in the heart. *J. Comp. Phys.* **25**, 220-252.
21. SHETH, K. & POZRIKIDIS, C. 1995 Effects of inertia on the deformation of liquid drops in simple shear flow. *Computers & Fluids.* **24**, 101-119.
22. SKELTON, R., HELTON, J., ADHIKARI, R., PINAUD, J., & CHAN, W. 2001 An introduction to the mechanics of tensegrity structures. To appear as a book chapter in *Handbook on mechanical systems design*.
23. XU, S., REMPFER, D., & LUMLEY, J. 2003 Turbulence over a compliant surface: numerical simulation and analysis. *J. Fluid Mech.* **478**, 11 - 34.